



# Simulations of Unsteady Three-Dimensional Hypersonic Double-Wedge Flow Experiments

John D. Reinertreine249@umn.edu\* and Graham V. Candlercandler@aem.umn.edu†

*University of Minnesota, Minneapolis, Minnesota 55455*

and

Jeffrey R. KomivesJeffrey.Komives@afit.edu‡

*U.S. Air Force Institute of Technology, Wright-Patterson Air Force Base, Ohio 45433*

<https://doi.org/10.2514/1.J058789>

Hypersonic flow over a three-dimensional 30–55 deg double wedge is investigated for three different conditions of varying enthalpy and Reynolds number with nitrogen as the test gas. Streamwise and spanwise wall heat flux are compared to the experimental data that were obtained at the University of Illinois at Urbana-Champaign and the California Institute of Technology. In previous studies, there were concerns that portions of the flowfield were rarefied; however, after an in-depth analysis, we find the flowfield to be firmly in the continuum regime. Comparisons of heat flux at an instant of time in the simulations show good agreement with the experiments. However, averaged heat flux over a long period of time relative to the experimental test time are underpredicted and develop low-frequency periodic motion. To better understand the unsteadiness and three-dimensionality of the flowfield, we analyze the mass flux through a spanwise plane, and we perform sparsity-promoting dynamic mode decomposition for the wall heat flux and midplane pressure. Finally, we analyze the effect of vibrational nonequilibrium on the flowfield. It is found that the flowfield dynamics vary with increasing enthalpy and Reynolds number. Furthermore, the flowfield is found to be three dimensional, unsteady, and asymmetric for all cases.

## Nomenclature

$C_F$	= nondimensional coefficient of shear stress
$C_H$	= nondimensional coefficient of heat flux
$C_P$	= nondimensional coefficient of pressure
$\bar{c}$	= mean thermal speed of gas, m/s
$e_{v\text{slip}}$	= vibrational energy at wall with slip condition
$e_{v\text{wall}}$	= vibrational energy at wall with no-slip condition
$H$	= height of double wedge (0.04620 m)
$Kn$	= Knudsen number
$Kn_{\text{GLL}}$	= gradient-length local Knudsen number
$L$	= characteristic length of double wedge (0.0508 m)
$L_g$	= gradient-length scale
$\dot{m}_b$	= span-binned mass flux, kg/s
$\dot{m}$	= mass flux, kg/s
$Pr$	= Prandtl number
$q$	= heat flux, W/m <sup>2</sup>
$R$	= gas constant
$T$	= temperature, K
$T_{\text{slip}}$	= temperature at wall with slip condition
$T_{\text{wall}}$	= temperature at wall with no-slip condition
$t$	= time, s
$t/\tau_f$	= nondimensional time
$U$	= $x$ direction velocity, m/s
$v_{t\text{slip}}$	= tangential velocity at wall with slip condition
$v_t$	= tangential velocity at wall with no-slip condition
$W$	= width of the double wedge (0.1016 m)
$x/L$	= $x$ direction normalized by characteristic length of double wedge

$y/H$	= $y$ direction normalized by height of double wedge
$z/W$	= $z$ direction normalized by width of double wedge
$\gamma$	= ratio of specific heats
$\partial/\partial n$	= wall normal derivative
$\lambda$	= mean free path
$\lambda_v$	= mean free path that characterizes transport of vibrational energy
$\mu$	= dynamic viscosity, (N · s)/m <sup>2</sup>
$\rho$	= density, kg/m <sup>3</sup>
$\sigma$	= accommodation coefficient
$\sigma_T$	= accommodation coefficient for temperature
$\sigma_v$	= accommodation coefficient for vibrational energy
$\tau$	= shear stress, N/m <sup>2</sup>
$\tau_f$	= flow time, s
$\nabla$	= gradient

## Subscript

$\infty$  = freestream

## I. Introduction

AMINAR shock/shock and shock/boundary layer interactions are important flow features encountered on inlet forebodies and deflected control surfaces of hypersonic vehicles. Unsteadiness and oscillations associated with these complex flow features can cause buffeting and need to be understood and characterized for vehicle design and control.

Flows containing laminar shock/shock and shock/boundary layer interactions have been found to be unsteady at certain conditions. In 1960, Maull [1] performed experiments for hypersonic flow over axially symmetric spiked bodies. It was found that certain ratios of spike length to body diameter produced oscillatory flow at a unit Reynolds number of  $6.69 \times 10^6 / \text{m}$ . Schrijer et al. [2,3] used particle image velocimetry and schlieren to investigate the flowfield for a 15–45 deg double ramp geometry in hypersonic flow at a unit Reynolds number of  $14.6 \times 10^6 / \text{m}$ . It was found that the flowfield was unsteady and three dimensional. The unsteadiness of the separation shock was attributed to the shear layer, while the unsteadiness of the bow shock was attributed to the reattachment region. Hashimoto [4] performed experiments for a hypersonic double-wedge flow at a unit Reynolds number of  $3.5 \times 10^6 / \text{m}$ . The flow was steady for

Received 1 August 2019; revision received 7 February 2020; accepted for publication 30 April 2020; published online 12 August 2020. Copyright © 2020 by John D. Reinert. Published by the American Institute of Aeronautics and Astronautics, Inc., with permission. All requests for copying and permission to reprint should be submitted to CCC at www.copyright.com; employ the eISSN 1533-385X to initiate your request. See also AIAA Rights and Permissions www.aiaa.org/randp.

\*Graduate Student, Department of Aerospace Engineering and Mechanics. Member AIAA.

†Professor, Department of Aerospace Engineering and Mechanics. Fellow AIAA.

‡Assistant Professor, Department of Aeronautics and Astronautics. Member AIAA.

25–40 deg and 25–50 deg double-wedge geometries but unsteady for the 25–68 deg double-wedge geometry. If the second wedge angle was increased beyond 68 deg, the transmitted shock would impinge normal to the surface of the second wedge and cause further unsteadiness.

Supersonic and hypersonic inlets can also exhibit unsteady oscillatory flow, which is often referred to as inlet buzz. Trapier et al. [5] performed a time-frequency analysis of supersonic inlet buzz at Mach 1.8 and 2.0. For the Mach 1.8 case, the inlet buzz was found to have a low frequency of  $\approx 18$  Hz. The Mach 2.0 case had the same low-frequency inlet buzz, but with an additional high-frequency inlet buzz at approximately 120 Hz. The low-frequency inlet buzz was triggered by separation on the compression ramp. The high-frequency inlet buzz was triggered by the presence of shear layers under the cowl lip. They also found that the inlet buzz phenomenon can be detected in advance, which means it can be prevented/controlled with the use of a control device. Soltani and Farahani [6] studied the effects of angle of attack on inlet buzz. They found that two types of inlet buzz were present at 135 and 470 Hz for an axisymmetric inlet at Mach 2 with 0 deg angle of attack. As the angle of attack increased, the instability amplitude and the shock displacement for the leeward side increased. Tan et al. [7] performed an experimental study of a hypersonic inlet. They found that during the high-frequency inlet buzz cycle a separated region at the duct entrance periodically shrinks and expands. During the low-frequency inlet buzz cycle, the separated region would burst and be swallowed by the inlet.

Computational studies for shock/shock and shock/boundary layer interaction have also been found to produce unsteady oscillatory flow. Olejniczak et al. [8] performed two-dimensional simulations with a constant first wedge angle of 15 deg and second wedge angles 40, 45, and 50 deg. It was found that second wedge angles greater than 50 deg resulted in an unsteady oscillatory process similar to that of Maull [1]. Three-dimensional simulations of laminar hypersonic shock wave/boundary layer interactions for a compression ramp by Brown et al. [9] not only found the flow to be unsteady but also three dimensional above a unit Reynolds number of  $0.685 \times 10^6/m$ . Further analysis of the bifurcation of the flowfield for compression ramps can be found in the work by GS et al. [10]. Unsteady, three-dimensional flow has also been found in oblique shock/boundary layer interaction by Hildebrand et al. [11] and Dwivedi et al. [12] and references within.

Recent experiments for a 101.6 mm double-wedge model (30–55 deg) have been carried out at the University of Illinois at Urbana-Champaign in the Hypervelocity Expansion Tube (HET) [13] (now located at the California Institute of Technology). Two experiments were run at Mach 7 with stagnation enthalpies of 2.1 and 8.0 MJ/kg, which will be referred to as the HET\_2.1 and HET\_8.0 cases, respectively. For the HET\_2.1 case with nitrogen as the test gas, the flow was found to be possibly unsteady with oscillations about the mean flow. The HET\_8.0 case with nitrogen as the test gas was found to be steady [14,15]. Concerns were raised that the test time of  $327 \mu s$  (12.7 flow times) was too short and did not allow the flowfield to develop completely. A flow time is defined as the amount of time a fluid particle takes to travel a characteristic length at the freestream flow speed. The experiment was extended by Knisely and Austin [16] to analyze the test time and spanwise effects of the double wedge. They tested the same double-wedge model with a stagnation enthalpy of 8.2 MJ/kg in the T5 reflected shock tunnel, which has test times of at least  $1000 \mu s$  (74.1 flow times) [16,17]. This will be referred to as the T5\_8.2 case later on in this Paper. The triple point was found to oscillate within an ellipsoid area with major diameter of 1.0 mm. They also found that there were no spanwise or three-dimensional effects up to  $z/W = 0.25$  off the centerline, where  $z$  is the spanwise direction and  $W$  is the width of the wedge ( $W = 101.6$  mm).

Simulations for a two-dimensional 30–55 deg double wedge using the HET\_2.1 and HET\_8.0 test conditions were performed by Komives et al. [18], Badr and Knight [19], and Knight et al. [20]. The simulations predicted the flow to be unsteady for both cases, which contrasted with the experimental results. To understand possible reasons for the discrepancies, three-dimensional finite-span double-wedge simulations were performed by Reinert et al. [21].

They found the flowfield was unsteady and three dimensional for both cases. Recent two-dimensional and three-dimensional time-accurate simulations for the HET\_8.0 case were performed by Hao et al. [22]. The three-dimensional simulations were performed for a double wedge with an infinite span. They found that the flowfield had not reached a steady state solution at the end of the experimental test time. The current Paper builds upon the work by Reinert et al. [21] and additionally investigates the flowfield for the T5\_8.2 case.

The objective of the current Paper is to analyze the flowfield for a 30–55 deg finite-span double wedge at different enthalpies and Reynolds numbers. The test cases investigated are the HET\_2.1, HET\_8.0, and T5\_8.2 cases. The first part of this Paper describes the numerical method and the grid convergence results. The second part reports the analysis of rarefied effects for the three cases. The third part presents results of the simulations at an instant of time with the experiment. Additionally, time-averaged heat flux is compared to the experiment. Time-averaged streamwise heat flux is underpredicted when compared to the experiment for all three cases. The time-averaged spanwise heat flux, which is only compared with T5\_8.2, is also underpredicted. The time-averaged heat flux results for HET\_2.1 and HET\_8.0 do not compare well with the experiment due to the low-frequency oscillations of the flowfield and the short test time of the experiment (327 and  $242 \mu s$ , respectively). Further analysis of the flowfields are carried out by investigating the mass flux through time and the effects of vibrational nonequilibrium.

## II. Experimental and Numerical Setup

### A. Flowfield Description

A schematic of high enthalpy flow over a 30–55 deg double wedge is shown in Fig. 1. As the flowfield is being established, the initial shock structure is only an oblique shock from the first wedge and a bow shock from the second wedge. The oblique shock impacts the bow shock and forms a transmitted shock. The transmitted shock creates an adverse pressure gradient in the attached flow along the first wedge, which in turn causes the downstream flow to separate. The separated flow exists at the intersection of the first and second wedges. A separation shock is created from the separated region and impacts the oblique shock. The two shocks coalesce and then impact the bow shock. This type of shock structure is similar to an Edney Type IV/V shock/shock interaction [23]. Because the features of the flow are coupled together, it takes approximately eight flow times to establish the shock structure based on the simulations. However, the separated region takes roughly 70 flow times to fully develop based on the simulations for the HET\_2.1, HET\_8.0, and T5\_8.2 cases. After the separated region is fully developed, a periodic unsteadiness arises in the flowfield. The separated region is observed to increase and decrease in size during a single oscillation of this periodic unsteadiness. HET\_2.1 and HET\_8.0 have characteristic flow times of 25.8 and  $13.3 \mu s$ , respectively. The T5\_8.2 case has a characteristic

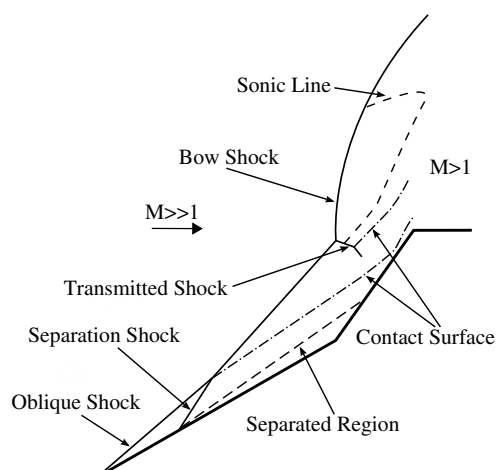


Fig. 1 Schematic diagram of the HET\_2.1 flowfield.

flow time of  $13.5 \mu\text{s}$ . The characteristic length is  $L = 50.8 \text{ mm}$  and corresponds to the length of the forward wedge face.

## B. Experimental Setup

The experiments were performed in the HET and the T5 reflected shock tunnel. The double-wedge model used in the experiments has 30–55 deg wedge angles and a span of 101.6 mm. Dimensions of the double wedge have been repeated in Fig. 2. The cases performed at the HET facility used nitrogen as the test gas at Mach 7 with enthalpies of 2.1 and 8.0 MJ/kg. The T5 experiment used nitrogen as the test gas at Mach 6.66 and a stagnation enthalpy of 8.2 MJ/kg. Note that the T5 test time was  $1000 \mu\text{s}$  (74.1 flow times), while the test times for HET\_2.1 and HET\_8.0 were only  $327 \mu\text{s}$  (12.7 flow

times) and  $242 \mu\text{s}$  (18.2 flow times), respectively. More information for the experimental cases is provided in Table 1.

## C. Numerical Method

The simulations were performed with US3D, an implicit finite volume unstructured grid flow solver [24,25]. The compressible Navier–Stokes equations are solved for thermochemical nonequilibrium flow. All cases were simulated for well over 100 flow times due to the slow development of the separated region. The wall temperature is initialized to 300 K, and we use an isothermal wall assumption because of the short test time.

The conservation of mass, momentum, and total energy equations are solved simultaneously. The internal energy equation is solved by calculating the vibrational energy using the simple harmonic oscillator model. Energy relaxation is calculated from the Landau–Teller model [26] using modified Millikan and White [27] relaxation rates and an additional modification from Park [28]. A detailed explanation of the vibrational and chemical relaxation rates is detailed by Candler and Nompelis [29]. The modified Steger–Warming flux splitting method [30] with a second-order MUSCL scheme is used to calculate the inviscid fluxes. A Crank–Nicolson second-order time integration method [31] was used for all cases unless otherwise stated. For the implicit time integration, four block-Jacobi type subiterations were performed for the implicit solve at each time step [32]. The block-Jacobi type subiterations were increased to 16, but no significant changes were observed in the flowfield.

## D. Grid Convergence

A bilaterally symmetric model of the double-wedge test article was used to create the grids. After smoothing, the grid was mirrored about the midplane. A fillet radius of  $10 \mu\text{m}$  was added to the top and sides of the double wedge in order to better simulate the flow around the edges. The radius was taken to be  $10 \mu\text{m}$ . The grid was generated using LINK3D, a hexahedral element grid generation software with a built-in parallel smoother. Figure 3 shows the grid at the surface and the midplane. Additionally, Fig. 3a shows the portion of the grid that is used as the wall boundary condition (i.e., no-slip boundary condition). Figure 4 shows the full computational domain for HET\_8.0 and T5\_8.2. The grid bounds were extended for the HET\_2.1 case due to concerns of subsonic flow exiting through the supersonic outflow boundary condition. The growth rate of the grid spacing near the wall is below 10%. The maximum near-wall  $y^+$  is less than 1 for all cases. The values for wall normal and spanwise spacing are provided in Table 2. Near the corners of the double wedge, the spanwise spacing was reduced to  $0.5 \mu\text{m}$  in order to resolve the flow features.

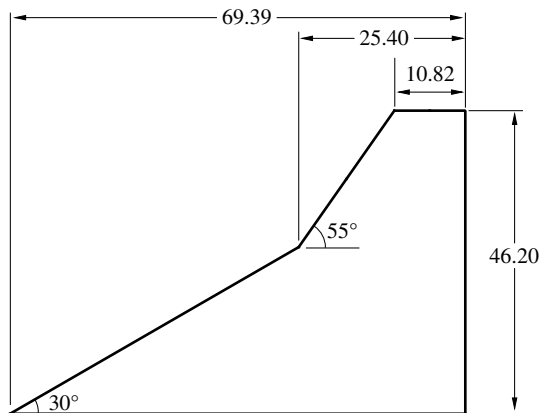
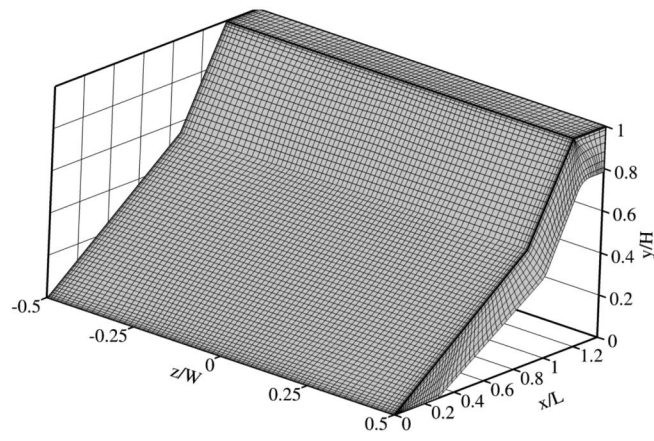


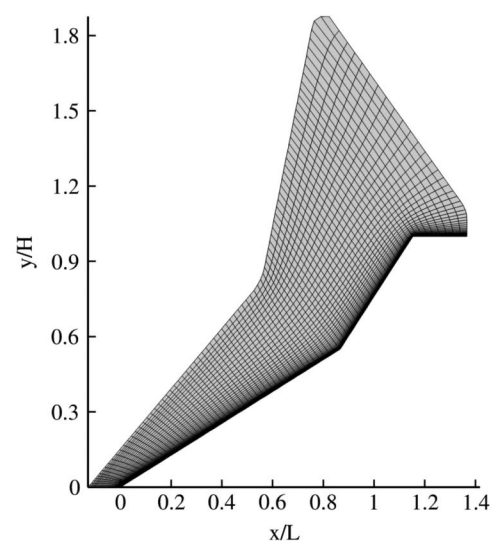
Fig. 2 Schematic of the double-wedge geometry with dimensions in millimeters. The width of the double wedge is  $W = 101.6 \text{ mm}$ .

Table 1 Freestream conditions [15,16]

Parameters	HET_2.1	HET_8.0	T5_8.2
Mach number	7.11	7.14	6.66
Static temperature, K	191	710	763
Static pressure, kPa	0.391	0.78	4.3
Velocity, m/s	1972	3812	3754
Density, kg/m <sup>3</sup>	0.0071	0.0038	0.0189
Unit Reynolds number, $10^6/\text{m}$	1.10	0.435	2.09
Stagnation enthalpy, MJ/kg	2.1	8.0	8.2
Experimental test time, $\mu\text{s}$	327	242	1000
Characteristic flow time, $\mu\text{s}$	25.8	13.3	13.5



a) Isometric view of the surface grid



b) Side view of the midplane grid

Fig. 3 Grid visualization with every fifth grid line shown. The  $xz$  coordinates are normalized by  $L = 0.0508 \text{ m}$ ,  $W = 0.1016 \text{ m}$ , and  $H = 0.04620 \text{ m}$ .

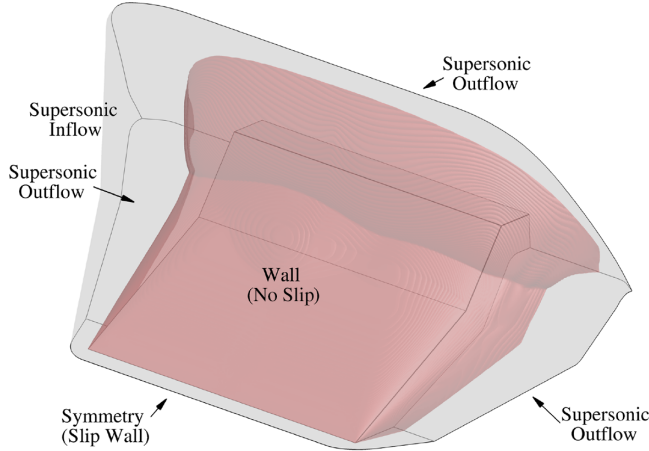


**Fig. 4 Computational domain with boundary conditions labeled. The red isosurface shows the instantaneous shock structure for HET\_8.0 at an arbitrary time greater than 100 flow times.**

**Table 2 Grid properties: values averaged over entire double wedge at an instant of time for the 60 million cell grid**

Parameters	HET_2.1	HET_8.0	T5_8.2
Wall normal spacing, m	$5.2 \times 10^{-7}$	$4.6 \times 10^{-7}$	$2.54 \times 10^{-8}$
Average spanwise spacing, m	$2.2 \times 10^{-4}$	$2.5 \times 10^{-4}$	$2.5 \times 10^{-4}$
Average $y^+$	0.061	0.130	0.027
Average $z^+$	16.334	32.181	131.453

Figure 5 shows the grid convergence for HET\_2.1 and HET\_8.0. The heat flux is calculated by averaging in the spanwise direction from  $-0.25$  to  $0.25 z/L$  from the centerline and then averaged through time from 150 to 350 flow times. The number of cells were increased equally in all three directions when going from 30 to 60 million and 60 to 120 million cell grids. Figure 5a shows that the 30 and 60 million cell grids do not match well near the peak heat flux. The 60 and 120 million cell grids match well at the separated region and the peak heat flux. Figure 5b shows that the heat flux for all three grids matches relatively well. Therefore, the results are grid converged for the 60 million cell grid. Because the enthalpies for HET\_8.0 and T5\_8.2 are relatively the same, we use the 60 million cell grid for T5\_8.2. All simulation results presented hereafter are performed with the 60 million cell grid.

### III. Confirmation of Continuum Regime

The numerical method assumes that the flowfield is continuum, which means the flow is in kinetic equilibrium. As a standard rule,

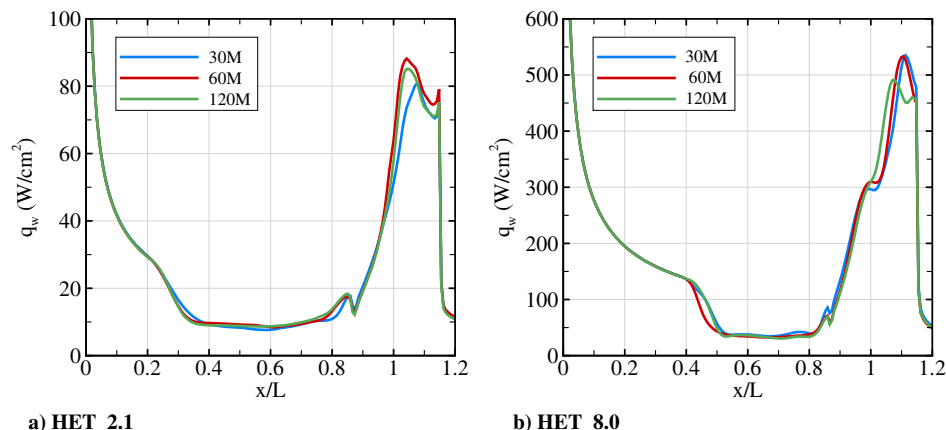


**Fig. 5 Grid convergence for HET\_2.1 and HET\_8.0. Heat flux was averaged in the spanwise direction from  $-0.25 \leq z/L \leq 0.25$  from the centerline and then averaged through time (150–350 flow times).**

the flow is in kinetic equilibrium if the Knudsen number  $Kn$  is below 0.01 [33]. The Knudsen number is a nondimensional number defined as  $Kn = \lambda/L$ , where  $\lambda$  is the mean free path and  $L$  is the characteristic length scale. The freestream Knudsen number based on the characteristic length scale  $L = 50.8$  mm is  $1.1 \times 10^{-5}$  for HET\_2.1,  $4.1 \times 10^{-4}$  for HET\_8.0, and  $8.2 \times 10^{-5}$  for T5\_8.2. Therefore, initial estimates show that the flowfield is likely in kinetic equilibrium. A less conservative gradient based length scale may also be used for computing the local Knudsen number in the flowfield. For a gradient-length local Knudsen number ( $Kn_{GLL} = \lambda/L_g$ ), the flow is considered to be in kinetic equilibrium if  $Kn_{GLL} < 0.05$  [34,35]. Here, we define the gradient-length scale as  $L_g = \rho/(|\nabla\rho|)$ , where  $\rho$  is the density. Figure 6 shows the Knudsen number calculated from the gradient-length scale for all three cases. It is clear that a continuum assumption holds well in these flow cases. The only location where  $Kn_{GLL} \geq 0.05$  is in the oblique shock. To further prove the flow is in kinetic equilibrium, Fig. 6 also shows the locations in the flowfield where  $0.01 \leq Kn_{GLL} < 0.05$ . From Fig. 6,  $Kn_{GLL}$  is above 0.01 only in the boundary layer near the leading edge in addition to the oblique, separation, and bow shocks. Additionally, because only a small region of the boundary layer has  $Kn_{GLL} \geq 0.01$  this suggests that velocity slip along the wall is insignificant at the leading edge for all three cases.

To verify that velocity slip for these flowfields is insignificant, we implemented a slip boundary condition for the wall. It is worth mentioning the effect of slip and nonequilibrium effects have been analyzed for a cylinder [36] and a sharp wedge [37]. Results for the sharp wedge showed that computational fluid dynamics (CFD) agreed well with direct simulation Monte Carlo (DSMC) at  $Kn = 0.002$ , which is an order of magnitude larger than the maximum freestream Knudsen number of the cases presented in this Paper. Also, Ref. [37] found that the percent difference of drag per unit length for CFD and DSMC was only 1.4% for  $Kn = 0.002$  for nitrogen.

For the slip boundary condition, the velocity slip and temperature jump at the surface of the body are calculated using the standard Maxwell model [38],

$$v_{\text{slip}} = \frac{2 - \sigma}{\sigma} \lambda \left. \frac{\partial v_t}{\partial n} \right|_{\text{wall}} \quad (1)$$

$$T_{\text{slip}} - T_{\text{wall}} = \frac{2 - \sigma_T}{\sigma_T} \frac{2\gamma}{(\gamma + 1)\Pr} \lambda \left. \frac{\partial T}{\partial n} \right|_{\text{wall}} \quad (2)$$

where  $v_{\text{slip}}$  is the tangential velocity and  $T_{\text{slip}}$  is the temperature at the surface (the slip conditions),  $T_{\text{wall}}$  is the temperature of the surface, and  $\lambda$  is the mean free path. The accommodation coefficients ( $\sigma$  and  $\sigma_T$ ) are assumed equal to 1.0.

To model the vibrational energy slip near the leading edge, we use an extension of the Maxwell model detailed by Gökçen [39],

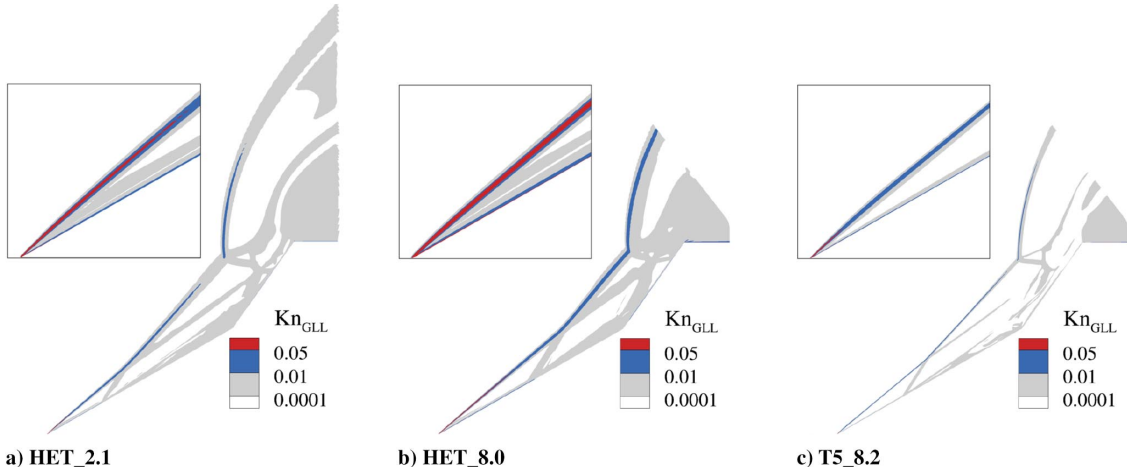


Fig. 6 Contour of the gradient-length local Knudsen number at midspan based on  $L_g$ . The HET\_2.1 and HET\_8.0 plots are taken at 172 and 151 flow times, respectively. The T5\_8.2 plot is taken at 150 flow times. The leading edge is magnified for all three plots.

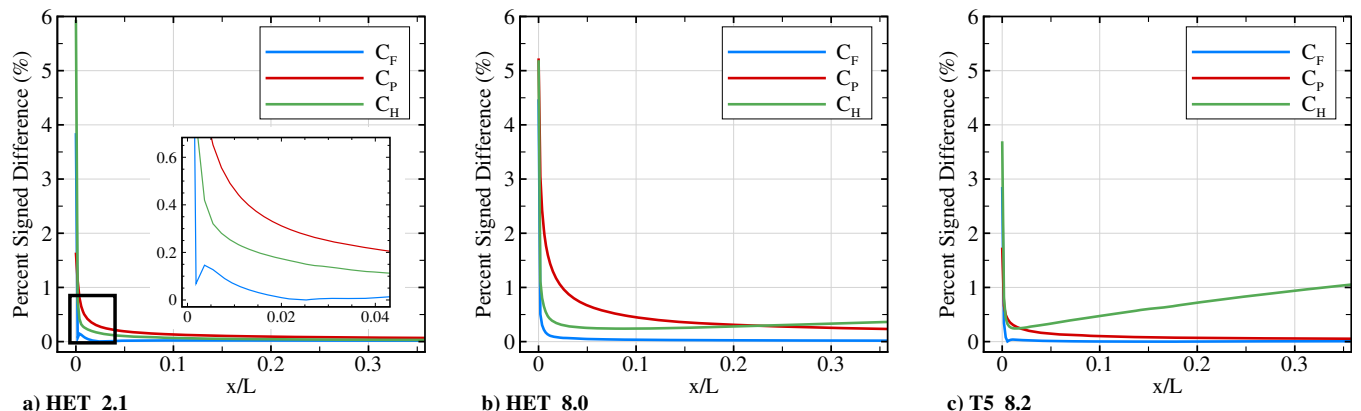


Fig. 7 Percent signed difference for nondimensional coefficients of viscosity, pressure, and heat flux near the leading edge for boundary conditions with and without slip. The no-slip boundary condition is used as the baseline. The  $x$  axis is nondimensionalized by  $L = 0.0508$  m.

$$e_{v\text{slip}} - e_{v\text{wall}} = \frac{2 - \sigma_v}{\sigma_v} \lambda_v \left. \frac{\partial e_v}{\partial n} \right|_{\text{wall}} \quad (3)$$

where  $\sigma_v$  is the accommodation coefficient for vibration and  $\lambda_v$  is the mean free path that characterizes transport of vibrational energy. We define  $\lambda_v = \lambda = 2\mu/\rho\bar{c}$ , where  $\bar{c} = \sqrt{(8RT/\pi)}$ . Candler et al. [40] analyzed the results for a hypersonic 25 deg cone using different values for  $\sigma_v$ . They found minuscule changes to the heat flux on the surface for  $\sigma_v < 0.3$ . Black et al. [41] measured  $\sigma_v = 0.001$  for stainless steel (type 321). The cases analyzed in this Paper used A2 tool steel for the double wedge; however, to our knowledge, no experimental measurements have been made for A2 tool steel. Therefore, we used a value of  $\sigma_v = 0.001$  for the simulations shown in Fig. 7. The percent difference for simulations with and without slip show small differences for nondimensional coefficients of shear stress, pressure, and heat flux [given by Eq. (4)]. The positive slope of the percent difference of  $C_H$  seen in Figs. 7b and 7c is due to the contribution of the vibrational energy to the overall wall heat flux. In the slip case, the vibrational energy contribution to the heat flux decreases with increasing distance from the leading edge, which is contrary to the no-slip case. Thus, the signed difference in heat flux between the slip and no-slip cases increases with distance from the leading edge. The domain was extended far beyond the separation front, and it was observed that  $C_H$  never exceeded a 2% difference. Therefore, the no-slip boundary condition at the leading edge is appropriate,

$$C_F = \frac{\tau}{(1/2)\rho_\infty U_\infty^2}, \quad C_P = \frac{p - p_\infty}{(1/2)\rho_\infty U_\infty^2}, \quad C_H = \frac{q}{(1/2)\rho_\infty U_\infty^3} \quad (4)$$

Finally, we can obtain an estimate for the number of cells that would be needed for a DSMC simulation. For this estimate, we focus on the HET\_8.0 case because it has the lowest density. Bird (Ref. [42] p. 216) recommends the DSMC cell dimension to be on the order of  $\lambda/3$ , where  $\lambda = \lambda(x, y)$  and represents the mean free path. We relax this recommendation to  $\lambda/2$ , which makes the area for a two-dimensional DSMC cell equal to  $(\lambda/2)^2$ . Then, we sum the area of the CFD cell divided by the area of the DSMC cell to obtain the number of DSMC cells required to perform a DSMC simulation. We estimate that  $4.60 \times 10^8$  DSMC cells are required for performing a two-dimensional DSMC simulation for HET\_8.0. If there are four DSMC particles per cell (which is the absolute minimum value before results become erroneous), then  $1.84 \times 10^9$  DSMC particles would be required. However, to get at least four DSMC particles per cell, the average number of DSMC particles per cell would need to be greater than 4. Previous two-dimensional studies have reported using  $4.88 \times 10^8$  DSMC cells with an average of 4.2 DSMC particles per cell in a larger two-dimensional computational domain than the current Paper [43]. Additionally, the two-dimensional DSMC simulation used 367,100 CPU hours. In comparison, two-dimensional CFD simulations use three CPU hours, and three-dimensional CFD simulations use 29,153 CPU hours to reach the same simulation time as the two-dimensional DSMC simulation.

In conclusion, performing a two-dimensional DSMC simulation for HET\_8.0 is not only computationally expensive but unnecessary because the flowfield is in kinetic equilibrium and velocity slip at the leading edge is inconsequential. Furthermore, in the next section, we show the flowfield is three dimensional. This means that for all three cases two-dimensional DSMC or CFD simulations disregard key flow physics.

#### IV. Results

In this section, we present the results for the HET\_2.1, HET\_8.0, and T5\_8.2 cases. First, we compare the instantaneous heat flux and shock structure to the experimental results at an instant of time. Second, we compare the time-averaged midspan heat flux results to the experiment for all three cases. Then, we compare the spanwise heat flux taken at  $0.786 x/L$  to the T5\_8.2 experimental results. Next, we calculate the time-averaged  $|\nabla\rho|$  for all three cases and compare the results to the HET experimental results. Additionally, we calculate the time-averaged wall heat flux for the full double wedge. For all three cases, the simulations qualitatively show the flowfields are unsteady and three dimensional. The time step was decreased by an order of magnitude for the HET\_2.1 case in order to ensure the unsteadiness was not a consequence of temporal resolution. The time step was decreased from 186 to 18.6 ns and resulted in the same unsteadiness. To quantify the unsteadiness and three-dimensionality, we analyze the mass flux through a spanwise plane that passes through the separated region. Finally, because these cases are at high enthalpy, we analyze the effect of vibrational nonequilibrium on the flowfield.

##### A. Comparison to Experiment

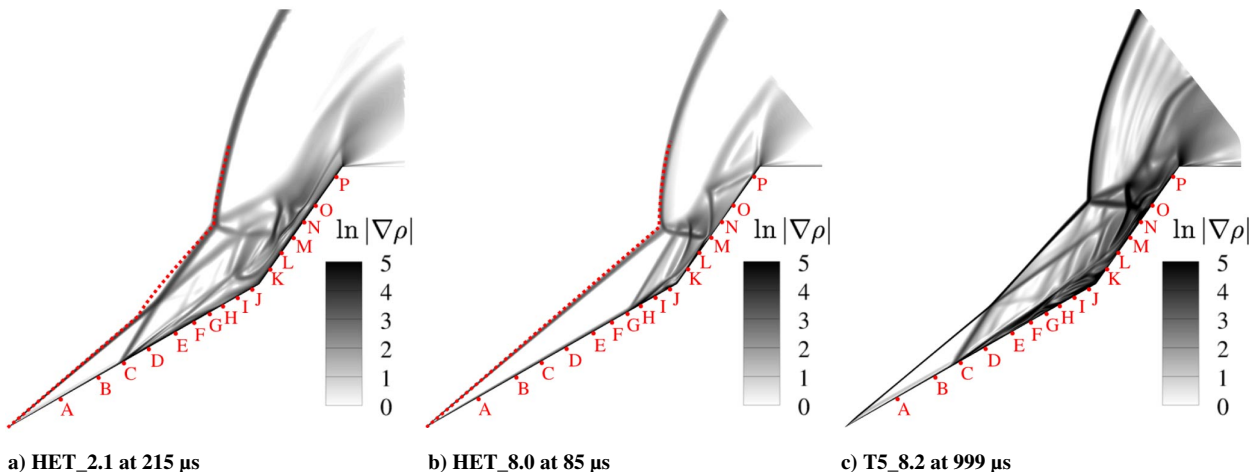
In this section, we compare wall heat flux for the three cases at an instant of time to the experiment. Simulations presented in this section were performed with second-order implicit Euler time integration for HET\_2.1 and HET\_8.0 because of numerical stability issues during initialization of the flowfield. We compare the shock structure and instantaneous heat flux at times approximately consistent with the experimental data. The simulation times do not match the experimental times because the simulations do not include the startup of the expansion tube. Based on the schlieren images, the HET simulations match well with the experiments at 215  $\mu\text{s}$  (8.3 flow times) for HET\_2.1 and 85  $\mu\text{s}$  (6.4 flow times) for HET\_8.0. Figure 8 shows  $\ln |\nabla\rho|$  contours with experimental schlieren. HET\_2.1 matches the experiment for the oblique shock, bow shock, and the triple point. However, the separation shock does not match near the oblique and separation shock interaction point. HET\_8.0 matches well with experiment for the oblique shock and bow shock. There is no interaction between the oblique shock and separation shock at this time in the simulation because the flowfield is still being established.

**Table 3 Normalized thermocouple locations: thermocouples A to J are located on the first wedge, thermocouples K to P are located on the second wedge, and bold font denotes thermocouples that were not installed for the HET cases**

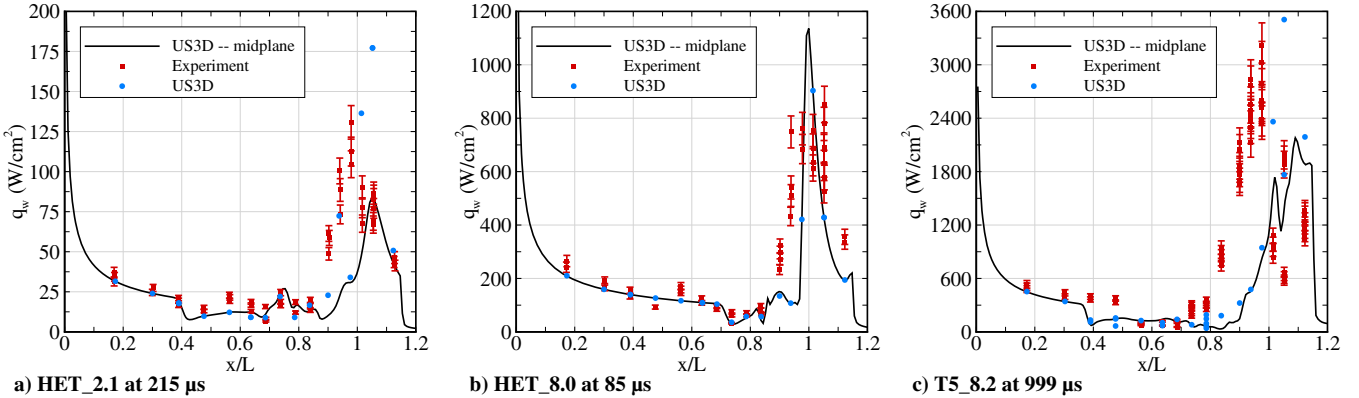
Thermocouple No.	Identification	$x/L$	$z/W$
1	A	<b>0.173</b>	0.0
2	B	0.3031	0.0
3	C1	0.390	0.0
4	C2	0.390	0.0405
5	D1	0.476	0.0
<b>6</b>	<b>D2</b>	<b>0.476</b>	<b>0.078</b>
<b>7</b>	<b>D3</b>	<b>0.476</b>	<b>0.15625</b>
8	E	0.563	0.0
9	F1	0.636	-0.0405
10	F2	0.636	0.0405
11	G	0.686	0.02025
12	H	0.736	0.0
13	I1	0.786	-0.02025
<b>14</b>	<b>I2</b>	<b>0.786</b>	<b>0.0625</b>
<b>15</b>	<b>I3</b>	<b>0.786</b>	<b>0.125</b>
<b>16</b>	<b>I4</b>	<b>0.786</b>	<b>0.1875</b>
<b>17</b>	<b>I5</b>	<b>0.786</b>	<b>0.25</b>
18	J	0.837	-0.0405
19	K	0.900	0.04625
20	L	0.938	0.023
21	M	0.976	0.0
22	N	1.014	-0.023
23	O1	1.052	-0.04625
24	O2	1.052	0.04625
25	P	1.123	0.0

Figure 8c does not have a comparison to the experimental schlieren because the schlieren images were not provided [16]. Therefore, 999  $\mu\text{s}$  (74.0 flow times) was chosen to compare with the experiment because it is close to the experimental time (1000  $\mu\text{s}$  or 74.1 flow times). In Fig. 8c, it is worth noting the oscillations of high and low  $\ln |\nabla\rho|$  behind the separation shock and the bow shock. This hints at a high-frequency disturbance in the flowfield.

Next, we compare the wall heat flux at the midplane with the thermocouple measurements from the experiment. The locations of each thermocouple are detailed in Table 3. Figure 8 shows the location of each thermocouple in the streamwise direction. The thermocouples are labeled alphabetically from A to P and correspond to increasing streamwise locations. Thermocouples A to J are located on the first wedge, and thermocouples K to P are located on the second wedge. Figure 9a shows that HET\_2.1 matches well before the separated region. Inside the separated region, the midplane heat flux is within 8% for thermocouples F, H, and J. For the shock impingement location, the peak heat flux is farther downstream than the experiment and is



**Fig. 8 Instantaneous contours of  $\ln |\nabla\rho|$  at midspan at an instant of time with experimental schlieren (red dotted line). Experimental data taken from Ref. [14].**



**Fig. 9 Heat flux at the midplane (black solid line) compared with the experimental values of heat flux (red symbols). Error bars are 8% of the heat flux values. Experimental data taken from Refs. [14] and [16]. The blue symbols are the spatially averaged heat flux over the surface area of each thermocouple.**

lower than the experiment. Figure 9b shows results for HET\_8.0. Before the separated region, the midplane heat flux is not within 8% at thermocouples A, D, E, and G. This is surprising because the simulation should match the heat flux of the laminar attached boundary layer. In the small separated region, the midplane heat flux matches within 8% at thermocouple H. At the shock impingement location, the peak midplane heat flux is overpredicted. It is worth mentioning that the experiment measures an unexpected jump in heat flux at thermocouple E. At this location, the heat flux should follow laminar boundary layer heating on the first wedge. Figure 9c shows the results for T5\_8.2. Before the separated region, the midplane heat flux matches well with thermocouples A and B. The predicted separation front is located at thermocouple C; however, the experiment measures the separation front at thermocouple E. In the separated region, the midplane heat flux matches well with the experimentally measured heat flux. The peak midplane heat flux is within 8% of the experimental peak heat flux; however, the location is predicted farther downstream than the experiment.

Overall, the midplane heat flux matches reasonably well with the experiment. However, comparisons made at the midplane are not entirely consistent. The thermocouple locations are not always at the midplane, and Fig. 10 shows that the heat flux on the wall is three dimensional. For example, the spatially averaged heat flux over the surface area of thermocouple O for HET\_2.1 is two times larger than the heat flux at the midplane. Therefore, a more appropriate comparison is to average the heat flux over each thermocouple surface area and compare the results to the experimentally measured heat flux.

Figure 9 shows the spatially averaged heat flux over the surface area of each thermocouple (shown with blue symbols). Figure 10

shows the three-dimensional heat flux on the surface of the double wedge and each thermocouple location. Referring to Fig. 9a, the spatially averaged heat flux matches thermocouples A, B, and C. Note that these thermocouples also match the midplane heat flux because the flow before the separated region is nominally two dimensional. We begin to see three-dimensionality in the separated region because the spatially averaged heat flux no longer matches the midplane heat flux. The spatially averaged heat flux matches better than the midplane at thermocouples G, J, and L; however, it overpredicts the peak heat flux at the shock impingement location. It is important to note the large differences of spatially averaged heat flux compared to midplane heat flux at the shock impingement location. Next, spatially averaged heat flux at thermocouple M drops below 40 W/cm<sup>2</sup>, but N and O jump to 135 and 177 W/cm<sup>2</sup>, respectively. It is also important to note that the spanwise paired thermocouples (C, F, and O), have the same spatially averaged heat flux. This shows that the flow is relatively symmetric about the midplane. However, this symmetry breaks down after 100 flow times (2580  $\mu$ s).

For HET\_8.0 (Fig. 9b), the spatially averaged heat flux does not deviate from the midplane heat flux. This shows that the flowfield is mostly two dimensional. Also, the flowfield is symmetric about the midplane because the spatially averaged heat flux of the spanwise paired thermocouples (C, F, and O) agree with each other. The heat flux is nominally two dimensional at 85  $\mu$ s because the separated region is still growing in size. Referring to Fig. 10b, the small separated region can be seen in dark blue near the intersection of the first and second wedges. The separation and bow shock are not interacting at this time in the simulation. However, the flowfield becomes asymmetric and three dimensional after 100 flow times

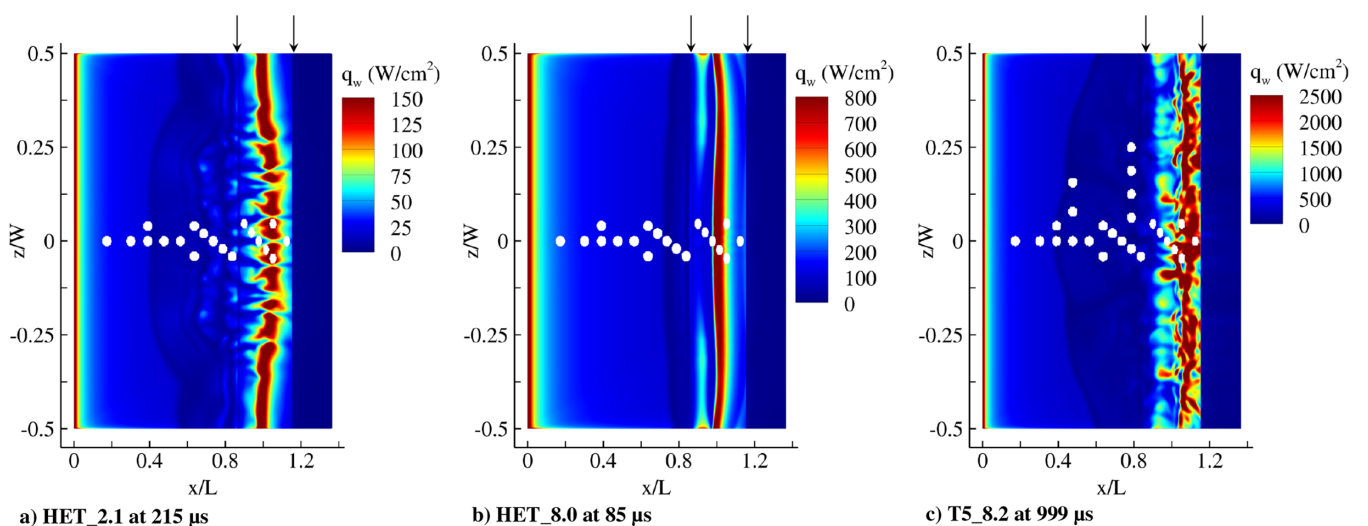


**Fig. 10 Heat flux at an instant of time; flow is from left to right. White dots are the thermocouple locations and have a diameter of 2.4 mm [16]. Black arrows denote the end of the first and second wedge.**

(1330  $\mu$ s) when the separation shock interacts with the oblique shock and bow shock.

For T5\_8.2 (Fig. 9c), before the separated region, the spatially averaged heat flux matches the midplane heat flux. Inside the separated region, the spatially averaged heat flux is closer to the experiment than the midplane heat flux at thermocouples C, F, and I. Additionally, we see three-dimensionality and asymmetry about the midplane inside the separated region and the shock impingement location because spanwise paired thermocouples C, D, F, I, and O have different heat flux values. Furthermore, thermocouples O1 and O2 differ by almost 100% (in both the simulation and the experiment), which shows that the flowfield is highly asymmetric about the midplane. Finally, Fig. 10c also shows the heat flux is asymmetric at the midplane and three dimensional at 999  $\mu$ s (74.0 flow times).

In conclusion, the midplane heat flux at the approximate test times compares well with the experimental data. However, because the wall heat flux shows that the flowfield is three dimensional, we calculate the heat flux over the surface area of each thermocouple. This spatially averaged heat flux compares better to the experiment than the midplane heat flux. In the next sections, we will present simulation results from 150 to 350 flow times and show that the flowfield is three dimensional, unsteady, and asymmetric about the midplane for all three cases.

## B. Time-Averaged Heat Flux

First, we analyze the time-averaged heat flux in the streamwise direction at the midplane. The time-averaged heat flux is calculated from 150 to 350 flow times. Figure 11 shows results for HET\_2.1, HET\_8.0, and T5\_8.2 compared with the experiment. For the HET\_2.1 case, the drop in heat flux due to the separated region is not as sharp as the instantaneous heat flux shown in Fig. 9a. The reason for this gradual slope is due to the separated region oscillating back and forth in the streamwise direction. The peak time-averaged

heat flux is farther downstream on the second wedge than the experiment. For the HET\_8.0 case (Fig. 11b), the slope at the separation front is still moderate compared to Fig. 9b. However, it is not as gradual as the time-averaged heat flux from HET\_2.1. This indicates the amplitude of the oscillations is not as large as the HET\_2.1 case. The peak time-averaged heat flux value and location is underpredicted and occurs farther downstream on the second wedge. For the T5\_8.2 (Fig. 11c), we see a gradual slope at the separation front similar to HET\_2.1. Additionally, the peak time-averaged heat flux matches well with the experiment. However, the peak heat flux location is farther downstream than the experiment.

Next, we analyze the spanwise effects. For the HET cases, the thermocouples farthest from the midspan were only 0.0405  $z/W$  from the centerline. For T5\_8.2, the farthest off midplane thermocouples are 0.25  $z/W$ . Therefore, we only compare the spanwise effects for T5\_8.2. Figure 12 shows the spanwise heat flux taken at 0.786  $x/L$ . Figure 12a shows the time-averaged heat flux from 150 to 350 flow times. The heat flux values are underpredicted compared to the experiment. The time-averaged heat flux range is 86 to 159  $W/cm^2$ . Figure 12b shows the instantaneous heat flux taken at 74 flow times and agrees slightly better than the time-averaged heat flux. Additionally, the instantaneous heat flux shows the sharp oscillations of heat flux present in the separated region. The range of heat flux for Fig. 12b is 18 to 228  $W/cm^2$ . Also, it is important to note the asymmetry and three-dimensionality of the time-averaged spanwise heat flux. Even after averaging over 200 flow times, the flowfield is asymmetric and three dimensional.

## C. Shock Structure

Figure 8 showed the natural logarithm of the density gradient magnitude ( $\ln |\nabla \rho|$ ) at an instant of time. In this section, we analyze the natural logarithm of the time-averaged density gradient magnitude  $\ln |\bar{\nabla} \rho|$  shown in Fig. 13. In this figure, the shock structure

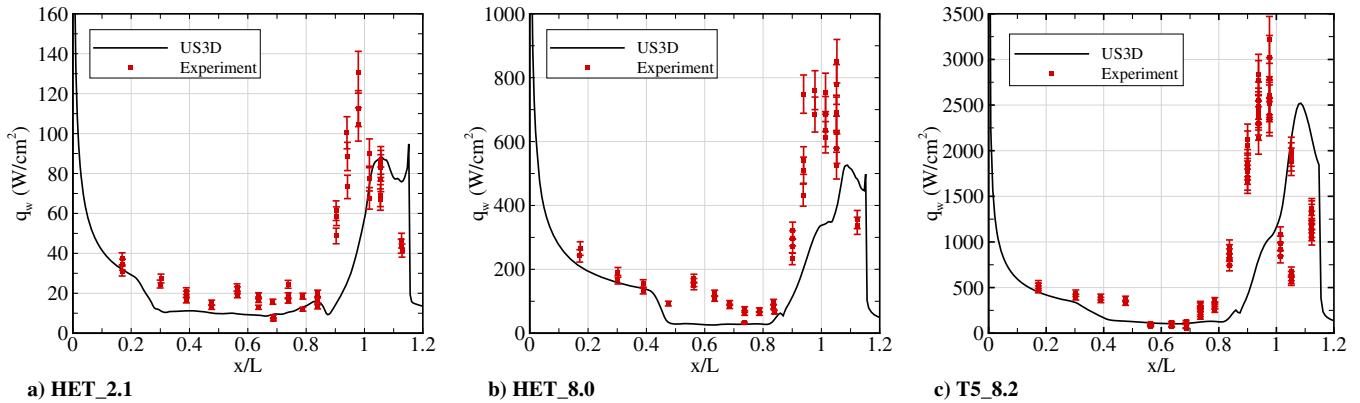


Fig. 11 Time-averaged heat flux from the simulation (black solid line) compared with the experimental values of heat flux (red symbols). Error bars are 8% of the heat flux values. Experimental data taken from Refs. [14] and [16].

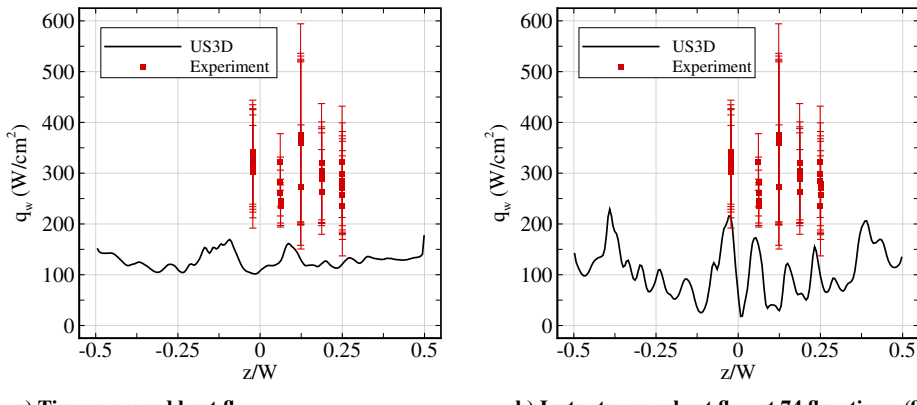


Fig. 12 T5\_8.2: spanwise heat flux at 0.786  $x/L$ . Data are taken from Ref. [16]. Error bars vary with each data point and range from 17 to 58%.

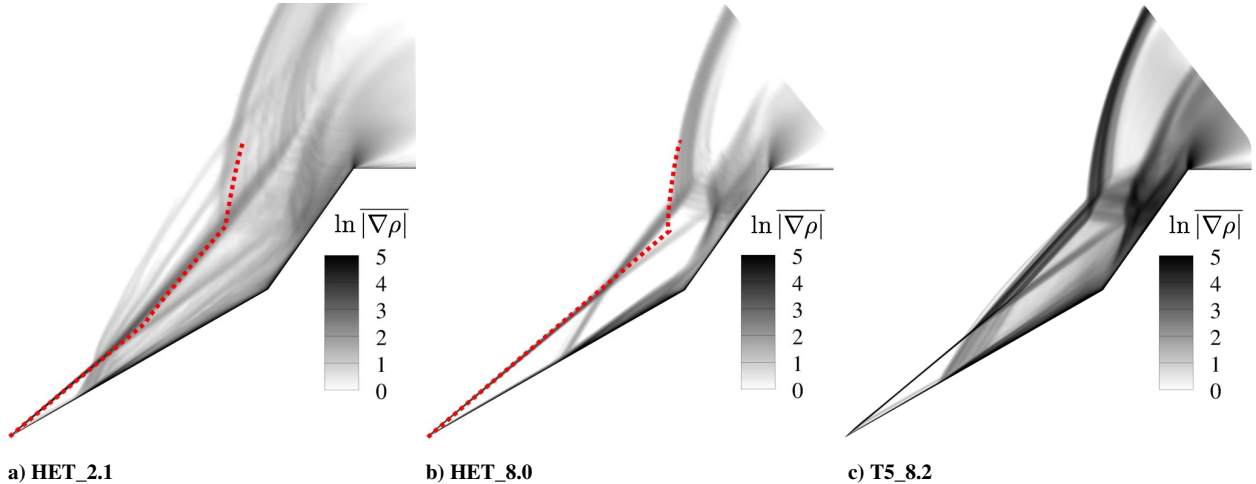


Fig. 13 Contour of the natural logarithm of time-averaged density gradient magnitude ( $\ln |\nabla \rho|$ ) at the midspan. All images were averaged from 150 to 350 flow times. The experimental schlieren is shown with a red dotted line.

appears blurry due to the unsteadiness of the flowfield. HET\_2.1 (Fig. 13a) has a well-defined oblique shock near the leading edge. However, the separated shock and bow shock are blurry due to the unsteadiness. The HET\_8.0 case (Fig. 13b) has a well-defined oblique shock, but the separated shock and bow shock are again blurry. The thickness of the bow shock is reduced in HET\_8.0, which means the unsteadiness of this case is less than HET\_2.1. The T5\_8.2 case has a well-defined shock structure, which illustrates the fact that this is the least unsteady of the three cases. Note that the separated shock and bow shock are well defined, but the triple point is slightly blurry. Recall that the experimental findings for T5\_8.2 were that the triple point oscillated within an ellipsoidal area with major diameter of 1.0 mm. The thickness of the triple point taken from Fig. 13c is approximately 4.6 mm.

Using the schlieren images presented in Ref. [14], we can overlay the  $\ln |\nabla \rho|$  images and compare the shock structure. Figure 13 compares the simulated shock structure to the experiment. The HET\_2.1 shock structure from the experiment lies within the  $\ln |\nabla \rho|$  contours. The HET\_8.0 shock structure agrees well with the simulation at the oblique shock and bow shock. However, the separated shock does not interact with the oblique shock and bow shock in the schlieren image provided by Swantek and Austin [14]. As stated in an earlier section of this Paper, this is due to the short test time of the expansion tube. Note that there is no T5\_8.2 comparison with experimental schlieren because schlieren images were not reported by Knisely and Austin [16].

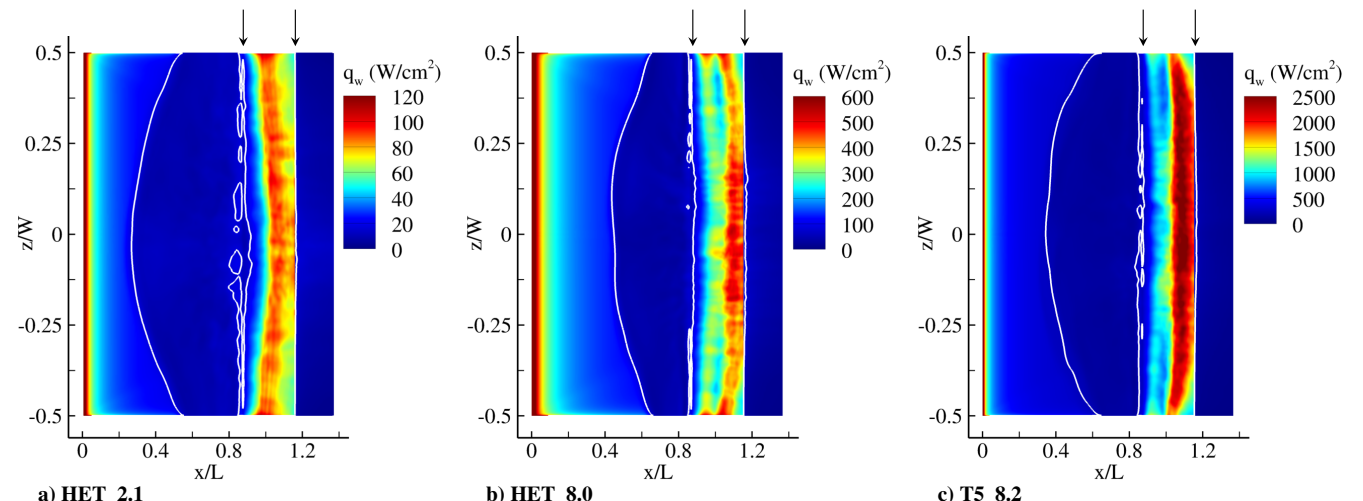


Fig. 14 Time-averaged heat flux from 150 to 350 flow times in  $\text{W}/\text{cm}^2$ . The flow is from left to right. The black arrows represent the edges of the first and second wedges.

#### D. Time-Averaged Three-Dimensional Wall Heat Flux

We further analyze the three-dimensionality by calculating the time-averaged wall heat flux (Fig. 14). The time average is calculated from 150 to 350 flow times. The separated region is largest in the HET\_2.1 case. In Fig. 14, the separated region is delineated by the white contour line, which has the value of  $17 \text{ W}/\text{cm}^2$  for HET\_2.1,  $80 \text{ W}/\text{cm}^2$  for HET\_8.0, and  $225 \text{ W}/\text{cm}^2$  for T5\_8.2. Note that the heat flux is symmetric and two-dimensional before the separated region and then becomes asymmetric and three dimensional at the separation front. This asymmetry and three-dimensionality continues downstream over the rest of the flowfield. As expected, the highest heating occurs at the shock impingement location on the second wedge.

#### E. Quantifying Unsteadiness

Until now, we have only presented qualitative results for the unsteadiness in the flowfield. In this section, we begin quantifying the unsteadiness by analyzing the integral of the mass flux through a spanwise plane. For HET\_2.1, the spanwise plane was taken at  $0.577 x/L$ . For HET\_8.0 and T5\_8.2, the spanwise plane was taken at  $0.722 x/L$ . These locations were chosen so that the spanwise plane would pass through the separated region. Figure 15 shows the span-binned mass flux  $\dot{m}_b$ ,

$$\dot{m}_b(x_0, z_i, t) = \int_{z_i-\Delta z}^{z_i+\Delta z} \int_{y_0}^{y_1} \rho u \, dy \, dz \quad (5)$$

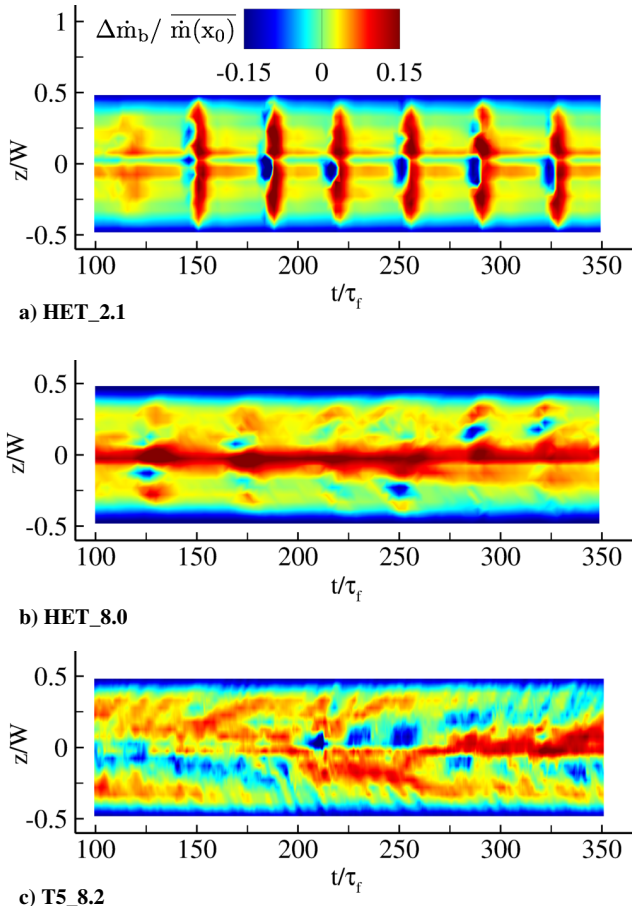


**Fig. 15** Span-binned mass flux contour normalized by the averaged mass flux through space for a given time, where  $\Delta\dot{m}_b = \dot{m}_b - \bar{\dot{m}}(x_0)$ . The x axis is nondimensionalized time from 100 to 350 flow times. The y axis is the nondimensionalized span from  $-0.5$  to  $0.5$   $z/W$ , where  $W = 101.6$  mm.

where  $\rho$  is the density,  $u$  is the velocity in the  $x$ -coordinate direction, and  $t$  is the time. The spatial coordinates are denoted by  $x$ ,  $y$ , and  $z$ . The streamwise location of the spanwise plane is denoted by  $x_0$ , and the spanwise locations of the bins are denoted by  $z_i$ . The half-width of a bin is  $\Delta z = 2.54$  mm. For HET\_2.1, Fig. 15a clearly shows the oscillation of the separated region. The regions of negative mass flux near  $z/W = 0$  occur when the separated region rapidly grows in size. The large streaks of positive mass flux occur when the separated region bursts and rapidly decreases in size. The regions between the large spikes in positive and negative mass flux represent the separated region slowly filling. For HET\_8.0 (Fig. 15b), an oscillation process of the separated region is visible; however, it is not as well defined as in the HET\_2.1 case. T5\_8.2 does not show a clear low-frequency oscillation process in the mass flux integration contour plot (Fig. 15c). However, a possible high-frequency oscillation process can be seen near the edges of the contour plot.

We can also analyze the mass flux integrated in the  $y$ - and  $z$ -coordinate directions:

$$\dot{m}(x_0, t) = \int_{z_0}^{z_1} \int_{y_0}^{y_1} \rho u \, dy \, dz \quad (6)$$

Figure 16 shows  $\dot{m}$  normalized by the mass flux averaged through space and time. The magnitude of this plot illustrates the strength of the oscillations. Figure 16 shows a low-frequency oscillation process for the HET\_2.1 and HET\_8.2 cases. The HET\_2.1 oscillation amplitude is an order of magnitude larger than the HET\_8.0 case. As expected, the T5\_8.2 does not show a low-frequency oscillation process.

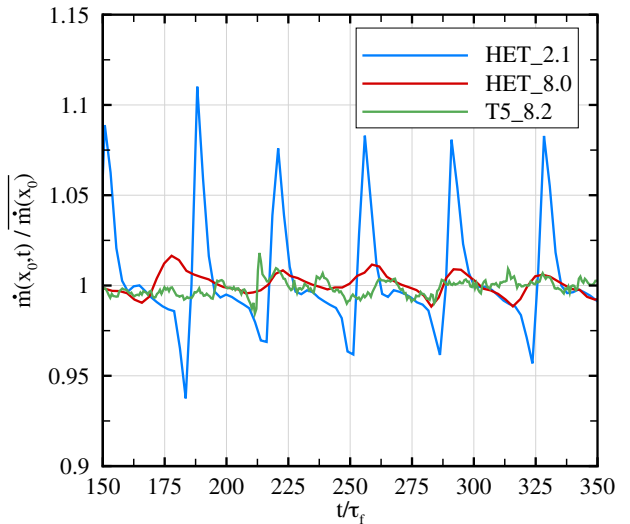


**Fig. 16** Mass flux normalized by the spatiotemporal averaged mass flux.

#### F. Spatiotemporal Analysis

In this section, we quantify the period of oscillation and investigate possible sources of unsteadiness of the flowfield. For this analysis we use a spatiotemporal analysis tool called sparsity-promoting dynamic mode decomposition (SPDMD) developed by Jovanović et al. [44]. Dynamic mode decomposition is a feature extraction technique that captures the coherent structures in the flowfield. The sparsity-promoting variant of dynamic mode decomposition (DMD) can help identify a subset of DMD modes that best approximate the flow dynamics. Additionally, SPDMD identifies the spatial location and temporal frequency of the dominant mode in an unsteady periodic flowfield. The spatial location of the dominant mode will indicate whether the mode exists within the separated region or the shear layer.

Sparcity is induced by using an  $l_1$  norm penalty term along with the standard least-squares deviation between the spatiotemporal simulation data and the linear combination of DMD modes. For details of the method, the reader is referred to the original paper. We use the code provided by the authors in Ref. [45]. It should be noted that only snapshots of two-dimensional planes were performed due to the memory requirements for performing DMD. However, recently, a new DMD algorithm that does not use singular value decomposition has been developed by Anantharamu and Mahesh [46] that allows for three-dimensional snapshots without the memory bottleneck.

Figure 17 shows the dominant mode for the HET\_2.1 case at the midspan and along the wall. Figure 17a shows the dominant mode found at the midplane visualized by pressure. The separated region is visible in blue, and the shock impingement location is in red. Figure 17b shows the dominant mode found along the wall visualized by wall heat flux. Again, we see a clear distinction of the separated region and shock impingement location. Because both modes occur at essentially the same frequency (only 0.6% difference), these can be categorized as the same mode. Additionally, because the same mode is seen in the midplane and along the wall, we hypothesize that the mode exists within the separated region. If the mode were in the shear layer, we would have only seen the mode in the midplane analysis and not in the wall analysis.

The period of an oscillation for HET\_2.1 is  $921 \mu\text{s}$  (35.7 flow times). Because the experimental test time for HET\_2.1 is only  $327 \mu\text{s}$  (12.7 flow times), the experiment would have been unable to observe this low-frequency oscillation. This highlights the main difficulty of performing high-enthalpy experiments for large wedge angles. Expansion tubes and reflected shock tunnels are the few experimental facilities that can reach enthalpies of  $2.1 \text{ MJ/kg}$  or greater. However, the test times for these facilities are small, and the large wedge angles require a substantial amount of time to establish the flowfield.

We also performed SPDMD for the HET\_8.0 and T5\_8.2 cases, but the results did not give a clear mode for the midspan pressure or

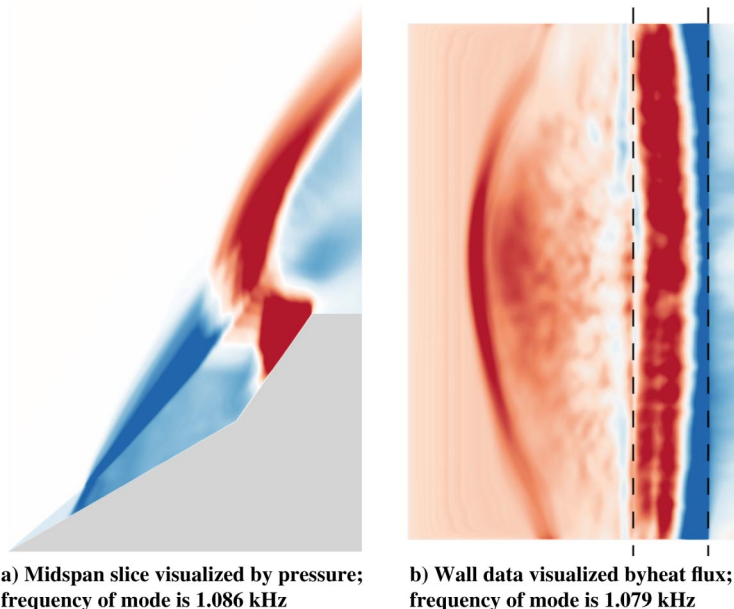


Fig. 17 HET\_2.1 dominant mode.

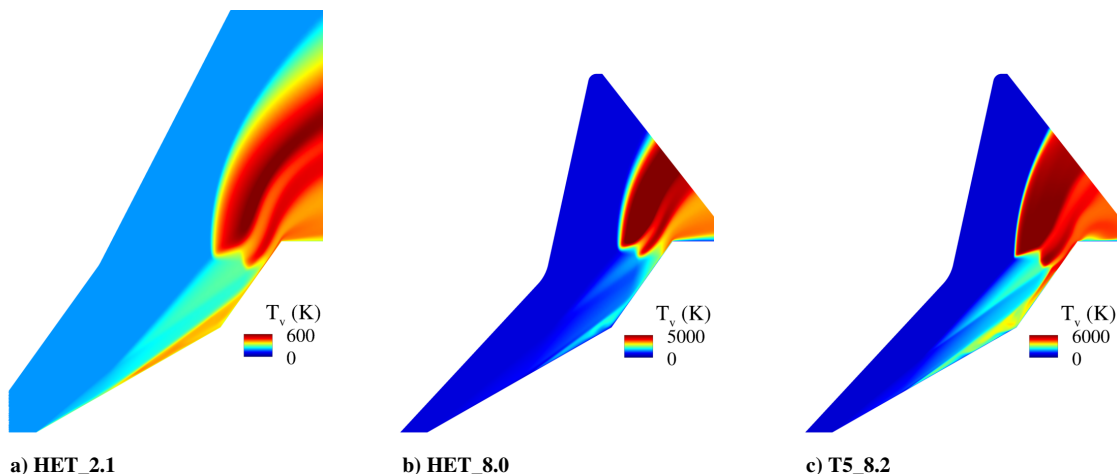


Fig. 18 Contour of the vibrational temperature (K) at midspan. The HET\_2.1 and HET\_8.0 plots are taken at 172 and 151 flow times, respectively. The T5\_8.2 plot is taken at 150 flow times.

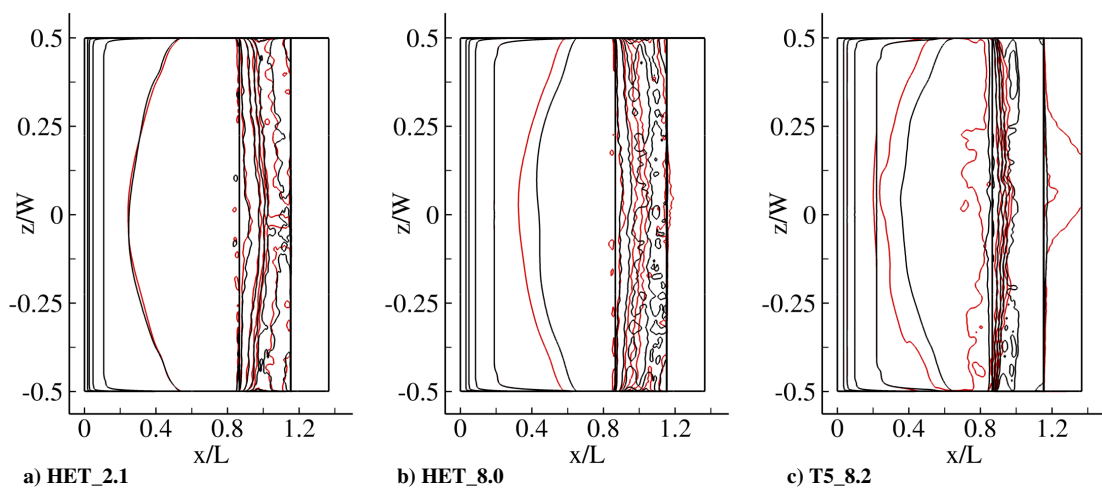


Fig. 19 Contour lines of the time-averaged wall heat flux from 150 to 350 flow times. Black lines are with vibrational nonequilibrium. Red lines are with thermal equilibrium.

wall heat flux. It is possible that the T5\_8.2 case has a dominant mode at a higher frequency than what was sampled. However, we leave this for future work.

### G. Analysis of Vibrational Nonequilibrium

In this section we analyze the effect of vibrational nonequilibrium on the flowfield. Figure 18 shows the vibrational temperature of the flowfield taken at an instant of time. The vibrational energy is highest after the bow shock. The regions of lowest vibrational energy are downstream of the oblique shock and above the separated region. From Fig. 18, the two shear layers downstream of the triple point can be seen.

Next, we analyze the effect of vibrational nonequilibrium on the three-dimensionality of the flowfield by qualitatively comparing the time-averaged heat flux for simulations with vibrational nonequilibrium to those with thermal equilibrium. Figure 19 shows time-averaged wall heat flux from 150 to 350 flow times. The black contour lines are the simulation results with vibrational nonequilibrium. The red contour lines are the simulation results with thermal equilibrium. The HET\_2.1 case is the least affected by vibrational nonequilibrium of the three cases. The separation fronts for HET\_2.1 with vibrational nonequilibrium and thermal equilibrium almost exactly match. HET\_8.0 and T5\_8.2 both show the separation front extending farther upstream than the vibrational nonequilibrium cases. Note that the simulations with vibrational nonequilibrium and with thermal equilibrium match exactly before the separated region, where the vibrational temperature is relatively low.

## V. Conclusions

Results from unsteady three-dimensional simulations of hypersonic flow with nitrogen gas over a finite span 30–55 deg double wedge are presented. Three freestream conditions corresponding to stagnation enthalpies of 2.1, 8.0, and 8.2 MJ/kg are considered. The simulations are found to be unsteady, three dimensional, and asymmetric in all cases.

This Paper validates the continuum analysis by analyzing the gradient-length local Knudsen number and implementing a slip boundary condition at the leading edge. This Paper finds that  $Kn_{GLL}$  remains below 0.05 for the overall flowfield, and the only locations where  $Kn_{GLL}$  is above 0.05 is a small region of the oblique shock. Additionally, a more stringent criterion of  $Kn_{GLL} > 0.01$  is only present in the boundary layer at the leading edge and the shock structure (oblique, separation, and bow shock). Furthermore, the results with the slip boundary condition differ by less than 2% compared to results with a no-slip boundary condition. Therefore, this Paper finds no evidence of rarefied effects for all three cases.

Instantaneous heat flux at the midplane is compared with the experimental measurements at times approximately consistent with the experimental data. It is found to match the experiment reasonably well. However, a more accurate comparison is also performed that calculates the spatially averaged heat flux over each thermocouple surface area. This spatially averaged heat flux matches better with the experiment. Furthermore, the time-averaged heat flux from 150 to 350 flow times is compared to the experiment. It is found to not match well with the experiment. However, this is expected because the short experimental test time would not have been able to capture the low-frequency unsteadiness.

The unsteadiness is quantified by the integrated mass flux through a spanwise plane. The HET\_2.1 case is the most unsteady of the three cases investigated. The T5\_8.2 case is the least unsteady and exhibits a different type of unsteadiness. The HET\_2.1 and HET\_8.0 cases have a characteristic low-frequency unsteadiness within the shock wave boundary layer system. These oscillations are associated with fill and burst of the separated region. A sparsity-promoting dynamic mode decomposition is performed for heat flux on the wall and pressure at the midplane. The frequency of the dominant oscillation mode is obtained for the HET\_2.1 case and is found to be roughly 1.08 kHz. A clear dominant oscillation mode is not found for the HET\_8.0 and T5\_8.2 cases. This could be due to competing three-dimensional instabilities in the separated region and shear layer.

The T5\_8.2 case has a higher-frequency unsteadiness than the other two cases. This oscillation process is unlikely associated with the separated region and is, instead, associated with the shear layer near the triple point.

Future experiments for double-wedge geometries should first perform preliminary simulations in order to determine flow establishment time, two-dimensionality, and steadiness of the flowfield. If the facility is an expansion tube or reflected shock tunnel, the angles of the first and second wedges should be relatively small so that a separated region does not exist at the intersection of the two wedges. This will reduce the establishment time of the flowfield, which is important for facilities that have a short test time. Additionally, this Paper has clearly shown that double-wedge flowfields can exhibit three-dimensionality, asymmetry about the midplane, and unsteadiness. Therefore, future computational simulations of high-enthalpy flowfields of double wedges should be performed for the full three-dimensional geometry.

## Acknowledgments

This Paper was sponsored by the Collaborative Center for Aerospace Sciences, the U.S. Air Force Office of Scientific Research under grant number FA9550-17-1-0250, and the U.S. Office of Naval Research under grant number N00014-15-1-2522. Thanks are due to Ioannis Nompelis for his insightful discussions on double-wedge and double-cone flowfields. Finally, special thanks are due to Anubhav Dwivedi; his guidance and support made this Paper possible. This material has been cleared for public release. Case Number 88ABW 2018-4081. This material is declared a work of the U.S. Government and is not subject to copyright protection in the United States. The views and conclusions contained herein are those of the authors and should not be interpreted as necessarily representing the official policies or endorsements, either expressed or implied, of the funding agencies or the U.S. Government.

## References

- [1] Maull, D. J., "Hypersonic Flow over Axially Symmetric Spiked Bodies," *Journal of Fluid Mechanics*, Vol. 8, No. 4, 1960, pp. 584–594. <https://doi.org/10.1017/S0022112060000815>
- [2] Schrijer, F., Van Oudheusden, B., Dierksheide, U., and Scarano, F., "Quantitative Visualization of a Hypersonic Double-Ramp Flow Using PIV and Schlieren," *12th International Symposium on Flow Visualization*, German Aerospace Center (DLR), 2006.
- [3] Schrijer, F., Caljouw, R., Scarano, F., and Van Oudheusden, B., "Three Dimensional Experimental Investigation of a Hypersonic Double-Ramp Flow," *Shock Waves*, Springer-Verlag, Berlin, 2009, pp. 719–724. [https://doi.org/10.1007/978-3-540-85168-4\\_116](https://doi.org/10.1007/978-3-540-85168-4_116)
- [4] Hashimoto, T., "Experimental Investigation of Hypersonic Flow Induced Separation over Double Wedges," *Journal of Thermal Science*, Vol. 18, No. 3, 2009, pp. 220–225. <https://doi.org/10.1007/s11630-009-0220-4>
- [5] Trapier, S., Deck, S., Duveau, P., and Sagaut, P., "Time-Frequency Analysis and Detection of Supersonic Inlet Buzz," *AIAA Journal*, Vol. 45, No. 9, 2007, pp. 2273–2284. <https://doi.org/10.2514/1.29196>
- [6] Soltani, M. R., and Farahani, M., "Effects of Angle of Attack on the Inlet Buzz," *Journal of Propulsion and Power*, Vol. 28, No. 4, 2012, pp. 747–757. <https://doi.org/10.2514/1.B34209>
- [7] Tan, H.-J., Sun, S., and Yin, Z., "Oscillatory Flows of Rectangular Hypersonic Inlet Unstart Caused by Downstream Mass-Flow Choking," *Journal of Propulsion and Power*, Vol. 25, No. 1, 2009, p. 138. <https://doi.org/10.2514/1.37914>
- [8] Olejniczak, J., Wright, M. J., and Candler, G. V., "Numerical Study of Shock Interactions on Double-Wedge Geometries," AIAA Paper 1996-0041, 1996. <https://doi.org/10.2514/6.1996-41>
- [9] Brown, L. M., Boyce, R. R., Nudford, N., and O'Byrne, S., "Intrinsic Three-Dimensionality of Laminar Hypersonic Shock Wave/Boundary Layer Interactions," AIAA Paper 2009-7205, 2009. <https://doi.org/10.2514/6.2009-7205>
- [10] GS, S., Dwivedi, A., Candler, G. V., and Nichols, J. W., "Global Linear Stability Analysis of High Speed Flows on Compression Ramps," AIAA

- Paper 2017-3455, 2017.  
<https://doi.org/10.2514/6.2017-3455>
- [11] Hildebrand, N., Dwivedi, A., Nichols, J. W., Candler, G. V., and Jovanović, M. R., "Sensitivity Analysis for the Control of Oblique Shock Wave/Laminar Boundary Layer Interactions at Mach 5.92," AIAA Paper 2017-4312, 2017.  
<https://doi.org/10.2514/6.2017-4312>
- [12] Dwivedi, A., Nichols, J. W., Jovanović, M. R., and Candler, G. V., "Optimal Spatial Growth of streaks in Oblique Shock/Boundary Layer Interaction," AIAA Paper 2017-4163, 2017.  
<https://doi.org/10.2514/6.2017-4163>
- [13] Dufrene, A., Sharma, M., and Austin, J. M., "Design and Characterization of a Hypervelocity Expansion Tube Facility," *Journal of Propulsion and Power*, Vol. 23, No. 6, 2007, pp. 1185–1193.  
<https://doi.org/10.2514/1.30349>
- [14] Swantek, A., and Austin, J., "Heat Transfer on a Double Wedge Geometry in Hypervelocity Air and Nitrogen Flows," AIAA Paper 2012-0284, 2012.  
<https://doi.org/10.2514/6.2012-284>
- [15] Swantek, A. B., and Austin, J., "Flowfield Establishment in Hypervelocity Shock-Wave/Boundary-Layer Interactions," *AIAA Journal*, Vol. 53, No. 2, 2015, pp. 311–320.  
<https://doi.org/10.2514/1.J053104>
- [16] Knisely, A. M., and Austin, J. M., "Geometry and Test-Time Effects on Hypervelocity Shock-Boundary Layer Interaction," AIAA Paper 2016-1979, 2016.  
<https://doi.org/10.2514/6.2016-1979>
- [17] Hornung, H. G., "Performance Data of the New Free-Piston Shock Tunnel at GALCIT," AIAA Paper 1992-3943, 1992.  
[https://doi.org/10.1007/978-3-642-77648-9\\_95](https://doi.org/10.1007/978-3-642-77648-9_95)
- [18] Komives, J. R., Nompelis, I., and Candler, G. V., "Numerical Investigation of Unsteady Heat Transfer on a Double Wedge Geometry in Hypervelocity Flows," AIAA Paper 2014-2354, 2014.  
<https://doi.org/10.2514/6.2014-2354>
- [19] Badr, M. A., and Knight, D. D., "Shock Wave Laminar Boundary Layer Interaction over a Double Wedge in a High Mach Number Flow," AIAA Paper 2014-1136, 2014.  
<https://doi.org/10.2514/6.2014-1136>
- [20] Knight, D., Chazot, O., Austin, J., Badr, M. A., Candler, G., Celik, B., de Rosa, D., Donelli, R., Komives, J., Lani, A., et al., "Assessment of Predictive Capabilities for Aerodynamic Heating in Hypersonic Flow," *Progress in Aerospace Sciences*, Vol. 20, April 2017, pp. 39–53.  
<https://doi.org/10.1016/j.paerosci.2017.02.001>
- [21] Reinert, J. D., GS, S., Candler, G. V., and Komives, J. R., "Three-Dimensional Simulations of Hypersonic Double Wedge Flow Experiments," AIAA Paper 2017-4125, 2017.  
<https://doi.org/10.2514/6.2017-4125>
- [22] Hao, J., Wen, C.-Y., and Wang, J., "Numerical Investigation of Hypervelocity Shock-Wave/Boundary-Layer Interactions over a Double-Wedge Configuration," *International Journal of Heat and Mass Transfer*, Vol. 138, Aug. 2019, pp. 277–292.  
<https://doi.org/10.1016/j.ijheatmasstransfer.2019.04.062>
- [23] Edney, B., "Anomalous Heat Transfer and Pressure Distributions on Blunt Bodies at Hypersonic Speed in the Presence of Impinging Shocks," Aeronautical Research Inst. of Sweden, FFA Rept. 115, Stockholm, 1968.
- [24] Nompelis, I., Drayna, T. W., and Candler, G. V., "Development of a Hybrid Unstructured Implicit Solver for the Simulation of Reacting Flows over Complex Geometries," AIAA Paper 2004-2227, 2004.  
<https://doi.org/10.2514/6.2004-2227>
- [25] Nompelis, I., Drayna, T. W., and Candler, G. V., "A Parallel Unstructured Implicit Solver for Hypersonic Reacting Flow Simulation," AIAA Paper 2005-4867, 2005.  
<https://doi.org/10.1016/B978-044452206-1/50047-1>
- [26] Vincenti, W. G., and Kruger, C. H., *Introduction to Physical Gas Dynamics*, Krieger, Malabar, FL, 1965, pp. 198–206.
- [27] Millikan, R. C., and White, D. R., "Systematics of Vibrational Relaxation," *Journal of Chemical Physics*, Vol. 39, No. 12, 1963, pp. 3209–3213.  
<https://doi.org/10.1063/1.1734182>
- [28] Park, C., *Nonequilibrium Hypersonic Aerothermodynamics*, Wiley, New York, 1990.
- [29] Candler, G. V., and Nompelis, I., "Computational Fluid Dynamics for Atmospheric Entry," *Non-Equilibrium Gas Dynamics—From Physical Models to Hypersonic Flights*, Von Kármán Institute for Fluid Dynamics Lecture Series, von Karman Inst., Rhode-Saint-Genese, Belgium, Sept. 2009, pp. 15.1–15.56.
- [30] Candler, G. V., Subbareddy, P. K., and Nompelis, I., "CFD Methods for Hypersonic Flows and Aerothermodynamics," *Hypersonic Nonequilibrium Flows: Fundamentals and Recent Advances*, AIAA, Reston, VA, 2015, pp. 203–237.  
<https://doi.org/10.2514/5.9781624103292.0203.0238>
- [31] Wright, M., Bose, D., and Candler, G. V., "A Data-Parallel Line Relaxation Method for the Navier-Stokes Equations," *AIAA Journal*, Vol. 36, No. 2, 1998, pp. 1603–1609.  
<https://doi.org/10.2514/2.586>
- [32] Wright, M. J., Candler, G. V., and Prampolini, M., "Data-Parallel Lower-Upper Relaxation Method for the Navier-Stokes Equations," *AIAA Journal*, Vol. 34, No. 7, 1996, pp. 1371–1377.  
<https://doi.org/10.2514/3.13242>
- [33] Boyd, I. D., "Computation of Hypersonic Flows Using the Direct Simulation Monte Carlo Method," *Journal of Spacecraft and Rockets*, Vol. 52, No. 1, 2015, pp. 38–53.  
<https://doi.org/10.2514/6.2013-2557>
- [34] Boyd, I. D., Chen, G., and Candler, G. V., "Predicting Failure of the Continuum Fluid Equations in Transitional Hypersonic Flows," *Physics of Fluids*, Vol. 7, No. 1, 1995, pp. 210–219.  
<https://doi.org/10.1063/1.868720>
- [35] Bird, G., "Breakdown of Translational and Rotational Equilibrium in Gaseous Expansions," *AIAA Journal*, Vol. 8, No. 11, 1970, pp. 1998–2003.  
<https://doi.org/10.2514/3.6037>
- [36] Lofthouse, A. J., Scalabrin, L. C., and Boyd, I. D., "Velocity Slip and Temperature Jump in Hypersonic Aerothermodynamics," *Journal of Thermophysics and Heat Transfer*, Vol. 22, No. 1, 2008, pp. 38–49.  
<https://doi.org/10.2514/1.31280>
- [37] Lofthouse, A. J., and Boyd, I. D., "Nonequilibrium Aerothermodynamics of Sharp Leading Edges," AIAA Paper 2009-1316, 2009.  
<https://doi.org/10.2514/6.2009-1316>
- [38] Schaaf, S. A., and Chambre, P. L., *Flow of Rarefied Gases*, Princeton Univ. Press, Princeton, NJ, 1966, pp. 34–35.
- [39] Gökçen, T., "Computation of Hypersonic Low Density Flows with Thermochemical Nonequilibrium," Ph.D. Dissertation, Dept. of Aeronautics and Astronautics, Stanford Univ., Stanford, CA, June 1989.
- [40] Candler, G. V., Nompelis, I., Druguet, M.-C., Holden, M. S., Wadham, T. P., Boyd, I. D., and Wang, W.-L., "CFD Validation for Hypersonic Flight: Hypersonic Double-Cone Flow Simulations," AIAA Paper 2012-0581, 2002.  
<https://doi.org/10.2514/6.2002-581>
- [41] Black, G., Wise, H., Schechter, S., and Sharpless, R. L., "Measurements of vibrationally excited molecules by Raman scattering. II. Surface Deactivation of vibrationally excited N<sub>2</sub>," *Journal of Chemical Physics*, Vol. 60, No. 9, 1974, pp. 3526–3536.  
<https://doi.org/10.1063/1.1681570>
- [42] Bird, G., *Molecular Gas Dynamics and the Direct Simulation of Gas Flows*, Oxford Univ. Press, New York, 1994, p. 216.
- [43] Tumuklu, O., Levin, D. A., and Theofilis, V., "On the Temporal Evolution in Laminar Separated Boundary Layer Shock-Interaction Flows Using DSMC," AIAA Paper 2017-1614, 2017.  
<https://doi.org/10.2514/6.2017-1614>
- [44] Jovanović, M. R., Schmid, P. J., and Nichols, J. W., "Sparsity-Promoting Dynamic Mode Decomposition," *Physics of Fluids*, Vol. 26, No. 2, 2014, Paper 024103.  
<https://doi.org/10.1063/1.4863670>
- [45] Jovanović, M. R., Schmid, P. J., and Nichols, J. W., *DMDSP—Sparsity-Promoting Dynamic Mode Decomposition*, 2013. <http://people.ece.umn.edu/users/mihailo/software/dmdsp/> [retrieved 6 Aug. 2020].
- [46] Anantharamu, S., and Mahesh, K., "A Parallel and Streaming Dynamic Mode Decomposition Algorithm with Finite Precision Error Analysis for Large Data," *Journal of Computational Physics*, Vol. 380, March 2019, pp. 355–377.  
<https://doi.org/10.1016/j.jcp.2018.12.012>

R. D. Bowersox  
 Associate Editor